Sequential Quenching to Predict Semiconductor Defect Concentrations from Formation & Migration Energies: The Case of CdTe:As Doping

K.A. Arnab[1], I. Chatratin[2], A. Janotti[2], and M.A. Scarpulla[1,3]

[1.] Department of Materials Science and Engineering, University of Utah, Salt Lake City, Utah 84112, USA

[2.] Department of Materials Science and Engineering, University of Delaware, Newark, Delaware 19716, USA

[3.] Department of Electrical and Computer Engineering, University of Utah, Salt Lake City, Utah 84112, USA

Supplementary Material

A step-by-step guide for reproducing the sequential quenching (SQ) calculations is provided in the associated GitHub repository[1]. The guide includes all required scripts and a pre-configured setup for CdTe. Full details of the framework are available in the main text and our previous paper[2].

Figure S1 provides expanded concentration profiles for defects excluded from the main text (Fig. 2(a)) due to their lower concentrations. Also, here the equilibrium with Te condition is included to show the opposite thermodynamic condition. While Cd_i acts as the main compensator under equilibrium with Cd, As_{Cd} acts as the main compensator under equilibrium with Te.

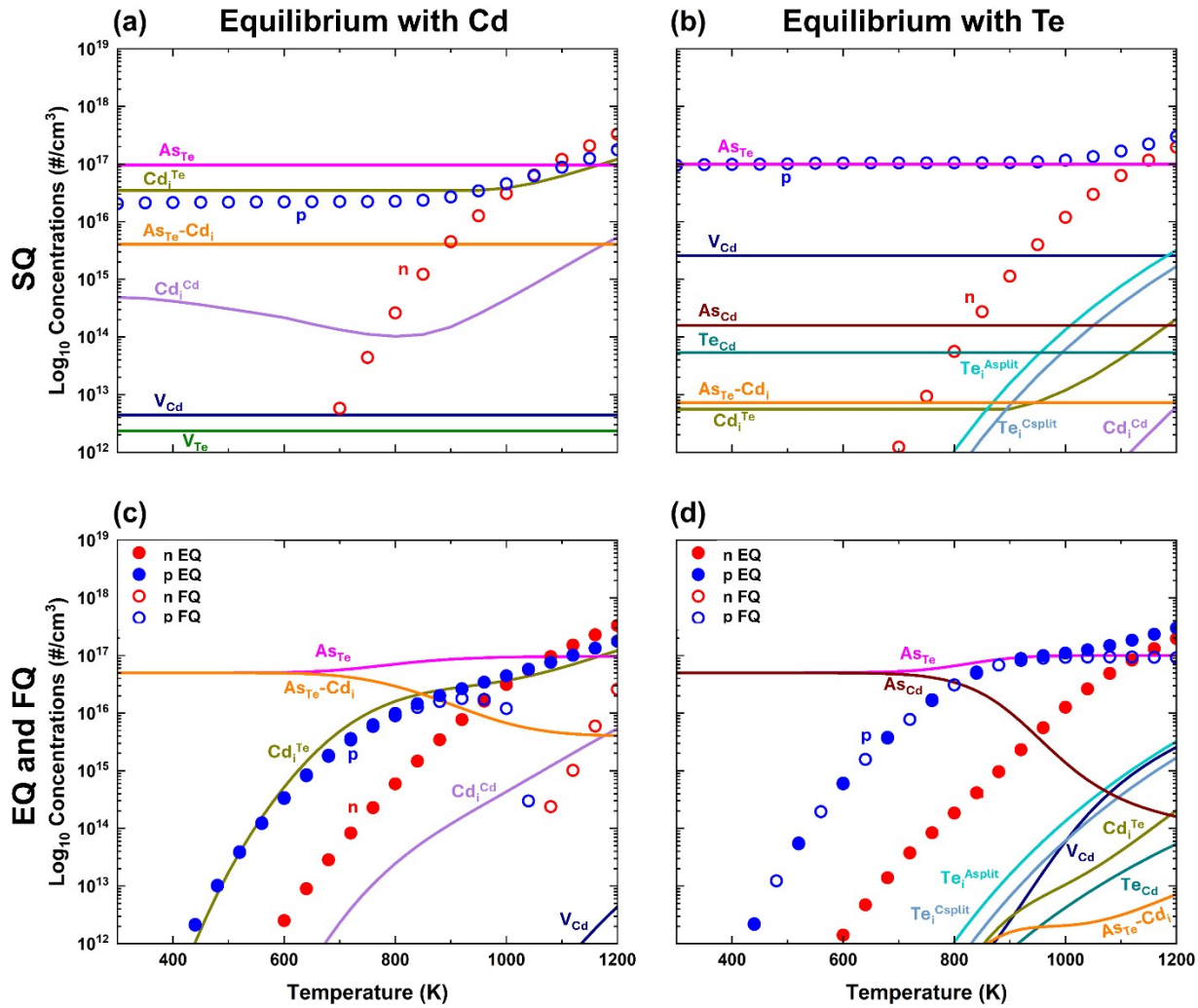

Figure S1: Defect concentrations as a function of temperature for CdTe equilibrium with Cd ((a) & (c)) and Te ((b) & (d)), comparing sequential quenching (SQ) calculations (characteristic distance = 1 μm & γ = 0.05 K/s) with equilibrium/full-quench (EQ/FQ) calculations. Panels (a) & (c) correspond to the same conditions shown in Figure 2(a) of the main text, but include detailed concentration profiles for minor defects under equilibrium with Cd case. Panels (b) & (d) extend the analysis to equilibrium with Te condition.

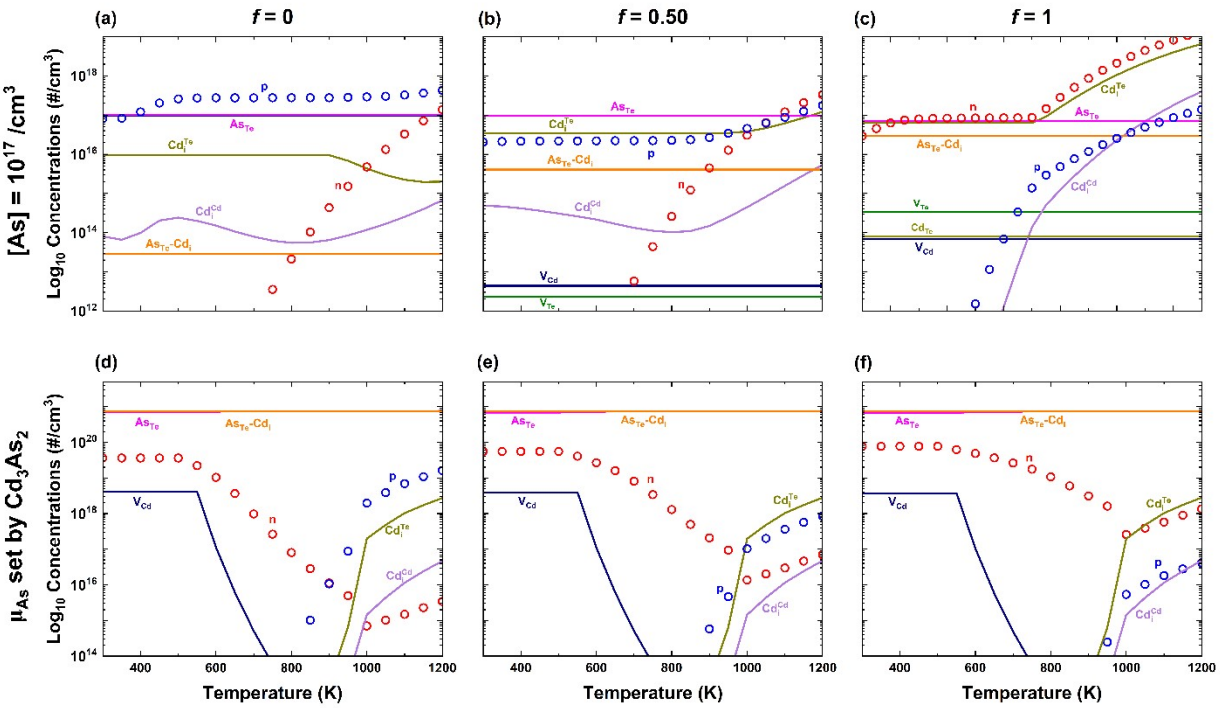

Figure S2: Defect concentrations as a function of temperature calculated for SQ scenario for CdTe equilibrium with Cd for varying *f* parameters (*f* = 0, 0.50, 1) (characteristic distance = 1 μm & γ = 0.05 K/s). Panels (a), (b) and (c) correspond to the SQ scenarios of Figure 2(a) of the main paper with varying *f* parameters. Panels (d), (e) and (f) correspond to the SQ scenarios of Figure 2(b) of the main paper with varying *f* parameters.

Figure S2 shows how parameter *f* affects the defect concentrations in SQ calculation. We can see changes in defect and carrier concentrations varying *f*. More conduction band dominance reduces hole concentration and increases electron concentration by increasing concentration of Cd_i.

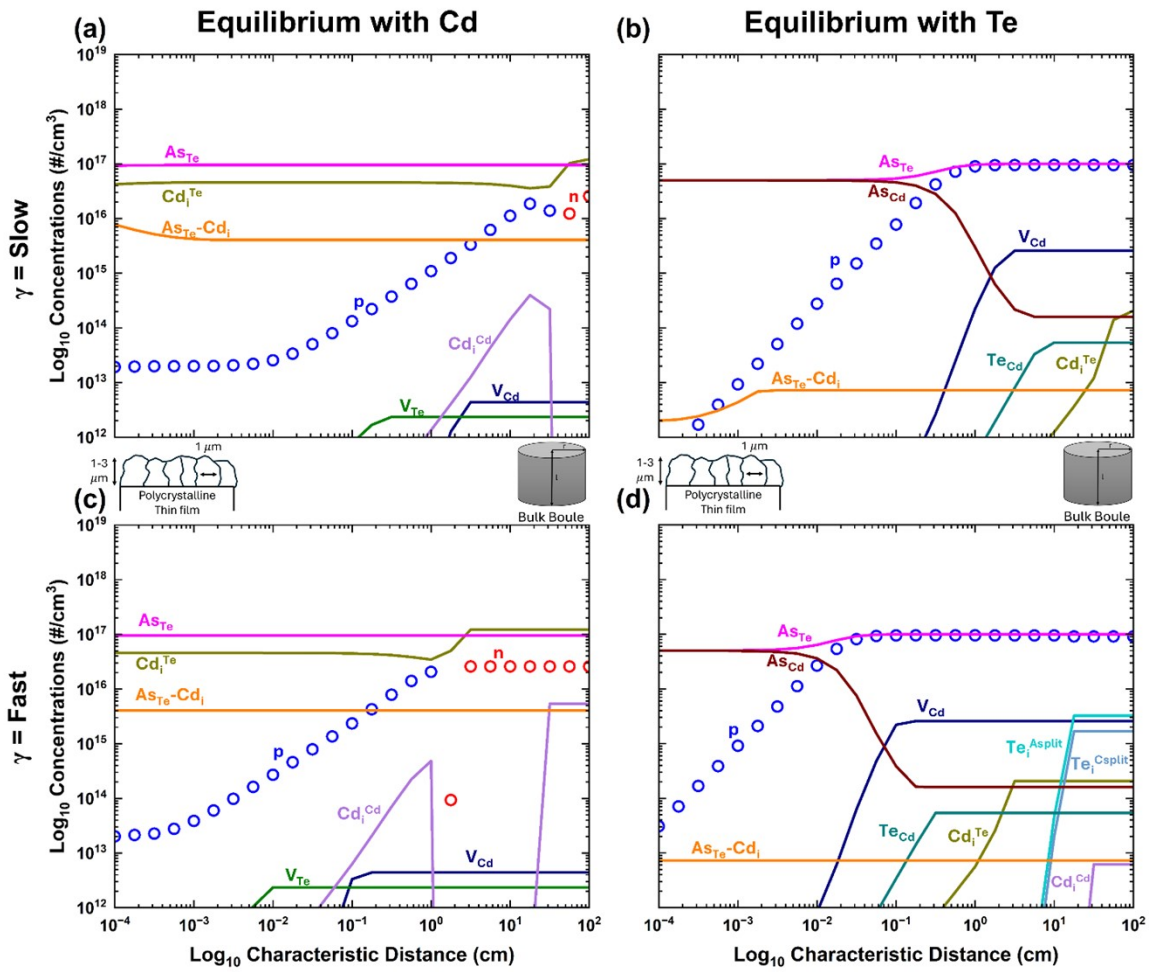

Figure S3: Expanded versions of the plots shown in Fig. 3(a) and 3(b) of the main text, including concentrations of all minor defects, to provide the complete defect population. Figure 3(a) corresponds to the combined representation of panels (a) and (c), while Fig. 3(b) corresponds to the combined representation of panels (b) and (d), respectively.

Figure S3 includes minor defect species that are omitted from the Fig. 3 ((a) & (b)) from the main text for clarity.

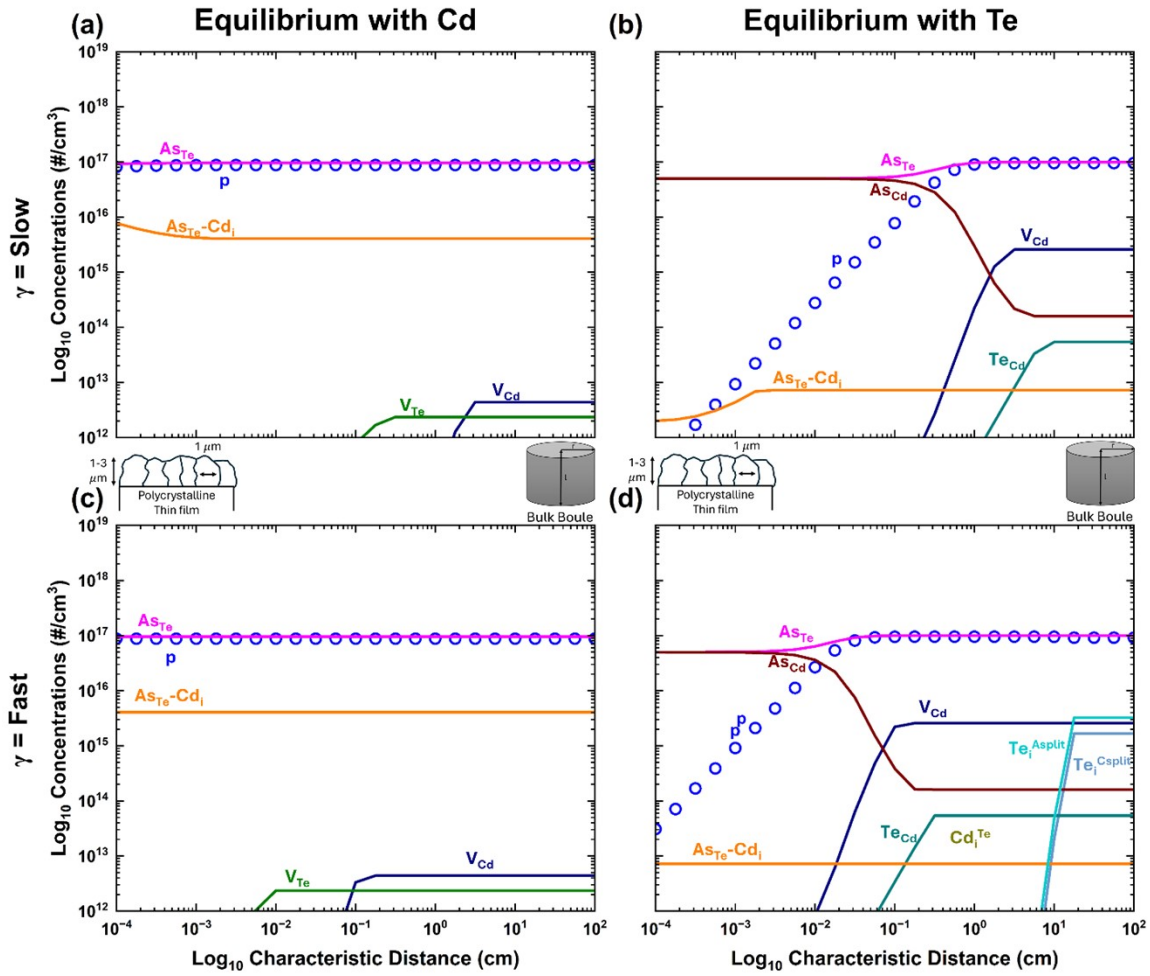

Figure S4: Expanded versions of the plots shown in Fig. 3(c) and 3(d) of the main text, including concentrations of all minor defects, to provide the complete defect population. Figure 3(c) corresponds to the combined representation of panels (a) and (c), while Fig. 3(d) corresponds to the combined representation of panels (b) and (d), respectively.

Figure S4 includes minor defect species that are omitted from the Fig. 3 ((c) & (d)) from the main text for clarity.

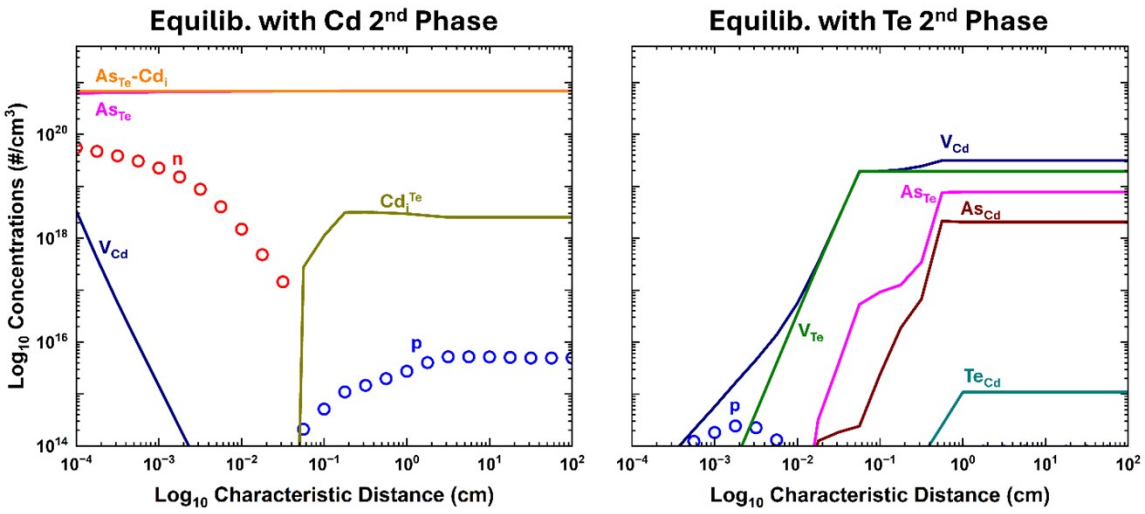

Figure S5: Similar to Fig. 3(a) and Fig. 3(b), but with μ_{As} determined by equilibrium with the secondary phases under Cd-rich (panel (a)) and Te-rich (panel (b)) conditions.

Figure S5 presents spatial defect and carrier profiles analogous to those shown in Figure 3(a) and 3(b) of the main text. While Figure 3 was calculated with μ_{As} determined by fixing the total arsenic concentration at [As] = 1×10^{17} cm^{-3}, Figure S4 shows results with μ_{As} constrained by equilibrium with secondary phases. Under Cd-rich conditions, Cd_3As_2 defines the secondary phase, whereas under Te-rich conditions, the relevant secondary phases are AsTe or As_2Te_3.

Equilibrium with the Cd-rich secondary phase (Cd_3As_2) produces strongly n-type behavior at small characteristic distances and weakly activated p-type behavior at larger characteristic distances. In contrast, equilibrium with Te-rich secondary phases (AsTe or As_2Te_3) results in substantially reduced arsenic activation, with only minimal p-type conductivity predicted across the characteristic-distance range.

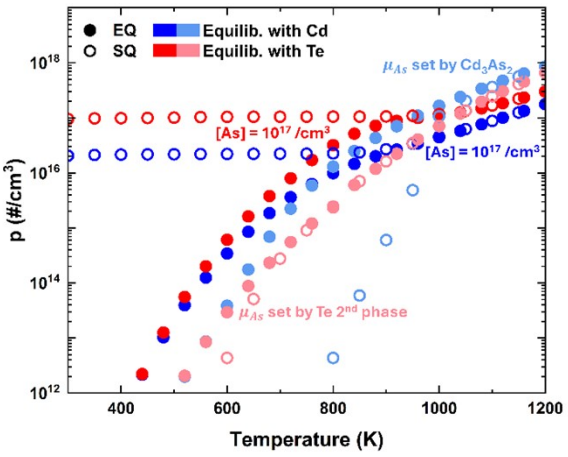

Figure S6: Temperature-dependent hole concentration, p(T), for the different calculation scenarios discussed in the main text and supplemental. All the p(T) trajectories are calculated for a 1 cm characteristic distance and a 0.05 K/s cooling rate with different μ_{As} conditions.

Figure S6 summarizes the evolution of hole concentration across the full temperature range for all modeled conditions and highlights differences in freeze-in behavior and dopant activation among the scenarios considered. The differences between EQ & SQ are also evident from the plot.

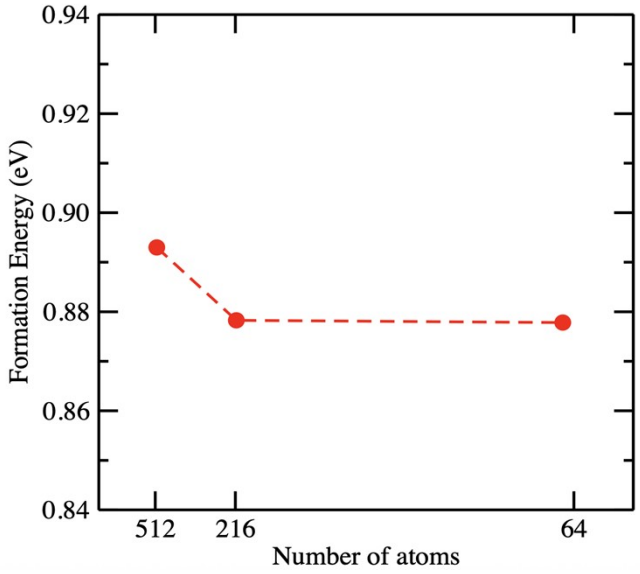

Figure S7: Supercell-size convergence of charged-defect formation energies. Corrected formation energies of representative charged As-related defects in CdTe calculated using 64-, 216-, and 512-atom supercells. The same finite-size correction and potential-alignment procedure was applied in each case. For As_{Te}^{-}, the corrected formation energy changes by less than 0.02 eV between the 216- and 512-atom cells, demonstrating that the 216-atom supercell used in the production calculations is sufficiently converged for the defect trends discussed in the manuscript.

Point defects and defect complexes were modeled in 216-atom supercells. Finite-size corrections and potential alignment were applied for charged defects. To assess the convergence with respect to supercell size, representative charged As-related defects were recalculated in 64-, 216-, and 512-atom supercells. The corrected formation energy of As_{Te}^{-} changes by less than 0.02 eV between the 216- and 512-atom cells, and similar convergence is obtained for $(As_{Te}\text{-}Cd_i)^{+}$. We therefore conclude that the 216-atom supercells are sufficient for the charged-defect energetics and trends discussed here.

References

1. GitHub - KROGER: Program for computing full and partial equilibria of point defects in solids, https://github.com/mikescarpulla/KROGER, (accessed September 15, 2024).
2. K. A. Arnab, M. Stephens, I. Maxfield, C. Lee, E. Ertekin, Y. K. Frodason, J. B. Varley and M. A. Scarpulla, *Phys. Chem. Chem. Phys.*, 2025, **27**, 11129–11143.